Knowledge & Innovation in Molecular and Industrial Applications (KIMIA)
Vol. 01, No. 1, June 2026, Page 32-46
E-ISSN XXX-XXXX

Characterization of Optical and Electronic Properties of Biocomposites Based on 2D Crystals (Reduced Graphene Oxide, MoS_2) and Biomacromolecules for Flexible Electronic Devices

Yuli Hardina[1]*,& Chantika Aditya Prameswari[2],
[1]*Universitas Negeri Padang, Indonesia, [2]Poltekkes Kemenkes Padang, Indonesia
*Co e-mail: yulihardinanasution@gmail.com[1]

Article Information
Received: August 10, 2026
Revised: October 10, 2026
Online: October 29, 2026

Keywords
Biocomposite, Reduced Graphene Oxide, MoS_2, Silk Fibroin, Flexible Electronics, Optical Band Gap

ABSTRACT
Flexible electronic devices require materials with mechanical compliance and tunable optoelectronic properties. This study developed reduced graphene oxide (rGO)-MoS_2/silk fibroin (SF) biocomposite films containing 0–2.0 wt% hybrid filler via solution casting. Structural, optical, and electrical properties were investigated using FTIR, XRD, UV-Vis spectroscopy with Tauc analysis, Raman spectroscopy, four-point-probe measurements, and repeated bending tests. FTIR revealed an increased β-sheet contribution, indicated by the amide I band shift from 1652 to 1622 cm^{-1}. XRD confirmed the formation of β-sheet (silk-II) structures and the presence of rGO and MoS_2 reflections. The optical band gap decreased from 4.42 to 2.35 eV, while the Raman D/G intensity ratio increased from 0.55 to 1.00, indicating increased defect density. The MoS_2 $E^1{}_2{}^g$–$A_1{}^g$ separation decreased from 26 to 21 cm^{-1}, suggesting thinner MoS_2 domains. Sheet resistance decreased by over four orders of magnitude, from 3.2×10^7 to 1.2×10^3 Ω/sq, with a percolation threshold near 1.0 wt%. Films containing 1.5–2.0 wt% filler maintained electromechanical stability after 1000 bending cycles, with resistance changes below 7.4%. These findings demonstrate the potential of rGO-MoS_2/SF biocomposites as tunable, bio-based materials for flexible electronics.

INTRODUCTION

The rapid growth of wearable sensors, foldable displays, and implantable bioelectronic devices has created sustained demand for active materials that remain mechanically compliant while retaining well-defined optical and electronic functionality. Conventional rigid semiconductors such as crystalline silicon cannot accommodate the bending, folding, and stretching required by these applications, which has motivated intensive research into two-dimensional (2D) crystals, including graphene and transition metal dichalcogenides such as molybdenum disulfide (MoS_2), as building blocks for flexible electronics (Díez-Pascual & Rahdar, 2022). Graphene offers high carrier mobility, broadband optical transparency, and mechanical

DOI: http://doi.org/10.69855/kimia
Available online at website: https://gpijournal.com/index.php/kimia

This work is licensed under a Creative Commons Attribution 4.0 International license

flexibility, whereas MoS_2 contributes a tunable, thickness-dependent band gap that transitions from indirect in bulk form to direct in monolayer form, giving rise to strong photoluminescence and layer-sensitive optoelectronic response (Lu et al., 2022).

In parallel, biomacromolecules such as silk fibroin, cellulose, and DNA have attracted growing interest as sustainable and biocompatible matrices for hybrid electronic materials (Wen et al., 2021). Silk fibroin (SF), a structural protein extracted from Bombyx mori cocoons, is particularly attractive because its secondary structure can transition between random-coil, α-helix, and β-sheet conformations depending on processing conditions, giving the material tunable mechanical stiffness, high optical transparency, and excellent film-forming ability (C. Li et al., 2022). Combining 2D crystals with biomacromolecules therefore offers a route toward biocomposites that merge the electronic and optical functionality of graphene and MoS_2 with the flexibility and low environmental footprint of bio-based polymers, a combination directly relevant to next-generation flexible and transient electronic devices (Azka et al., 2025). Because the incorporation of rGO and MoS_2 does not necessarily preserve the biodegradability of silk fibroin, the composites in this study are described as bio-based, and their biodegradation was not evaluated.

Several studies have explored graphene-silk fibroin hybrids for electronic and biosensing applications. Nilogal et al. (2021) fabricated conductive in situ reduced graphene oxide-silk fibroin bionanocomposites and reported a substantial increase in electrical conductivity as the graphene oxide content increased, attributing the effect to the formation of continuous conductive pathways within the protein matrix. Bhattacharya and Kaplan (2022) engineered silk-elastin-like proteins with a graphene oxide-binding domain to create dynamic hybrid materials for biomaterial-based electronic switches, demonstrating that genetically tunable protein-graphene interfaces can modulate electronic behavior. Xu et al. (2022) reviewed the composites of silk fibroin and graphene-based materials and highlighted that the incorporation ratio of graphene oxide strongly governs the trade-off between electrical conductivity and the biocompatibility or biodegradability of the resulting composite. Deng et al. (2022) further showed that microphase structure in silk fibroin-based biocomposites can be tuned via ionic liquid processing, influencing both mechanical and optical properties.

On the inorganic filler side, Mahmud and Islam (2023) fabricated a ternary nanocomposite of plasticized starch, reduced graphene oxide, and MoS_2, reporting that the addition of MoS_2 nanofiller reduced the optical band gap of the biopolymer matrix from 4.71 to 2.90 eV while simultaneously increasing specific capacitance and reducing charge-transfer resistance, which the authors attributed to enhanced interlayer charge transfer and the introduction of defect states. Lu et al. (2022) demonstrated, using machine-learning-assisted analysis, that the correlation between Raman and photoluminescence signatures in monolayer MoS_2 provides a reliable, non-destructive means of probing layer number, strain, and doping, which motivates the joint use of Raman and optical spectroscopy in composite characterization. Seydibeyoğlu et al. (2023) and Azka et al. (2025) reviewed hybrid nanocellulose/graphene and nanocellulose-only biopolymer composites for electronic applications and both emphasized that filler loading, dispersion quality, and filler-matrix interfacial interaction are the dominant factors controlling the electronic performance of biopolymer-based composites.

This work is licensed under a Creative Commons Attribution 4.0 International license

Despite this body of work, most existing studies examine either a graphene/biopolymer binary system or an inorganic ternary system based on a synthetic polymer matrix; comparatively few studies combine reduced graphene oxide (rGO) and MoS_2 as a hybrid 2D filler within a protein-based biomacromolecule matrix while jointly characterizing both optical (UV-Vis/Tauc, Raman) and electronic (sheet resistance, bending stability) properties within a single, systematically varied composition series. This study addresses that gap by (1) fabricating silk fibroin films incorporating an rGO-MoS_2 hybrid filler across a systematic loading series (0–2.0 wt%), (2) characterizing the resulting structural, optical, and electronic properties using FTIR, XRD, UV-Vis/Tauc analysis, and Raman spectroscopy, and (3) evaluating the electrical conductivity and electromechanical bending stability of the biocomposite films to assess their suitability for flexible electronic device applications.

METHODS

Bombyx mori silk cocoons were used as the source of silk fibroin (SF). Graphite powder and molybdenum disulfide (MoS_2) powder (99% purity, <2 µm particle size) were used as the precursors for the 2D crystal filler. Sodium carbonate (Na_2CO_3), lithium bromide (LiBr), sulfuric acid (H_2SO_4), potassium permanganate ($KMnO_4$), hydrogen peroxide (H_2O_2), and hydrazine hydrate were used for graphene oxide synthesis and reduction. All chemicals were of analytical grade and used without further purification.

Synthesis of GO and Exfoliated MoS_2

Graphene oxide (GO) was synthesized from graphite powder using a modified Hummers' method (Hummers & Offeman, 1958) involving oxidation with $KMnO_4$ in concentrated H_2SO_4, followed by exfoliation via ultrasonication. Briefly, 1 g of graphite powder was added to 23 mL of concentrated H_2SO_4 under stirring in an ice bath. Then, 3 g of $KMnO_4$ was slowly added while keeping the temperature below 20 °C. The mixture was then heated to 35 °C and stirred for 2 h, followed by the slow addition of 46 mL of deionized water. The reaction was terminated by adding 140 mL of deionized water and 10 mL of 30% H_2O_2, turning the suspension bright yellow. The product was washed repeatedly with 1 M HCl and deionized water until the pH reached ~6, then dried at 60 °C for 24 h. The resulting GO was exfoliated in deionized water by ultrasonication at 200 W for 2 h in an ice bath, followed by centrifugation at 8000 rpm for 30 min to remove unexfoliated particles. The supernatant containing single- to few-layer GO was collected and dried for further use.

MoS_2 nanosheets were obtained through liquid-phase exfoliation of bulk MoS_2 powder in N-methyl-2-pyrrolidone (NMP) at an initial concentration of 10 mg/mL under ultrasonication for 8 h using a bath sonicator (200 W, 40 kHz) with temperature maintained below 30 °C by circulating cooling water. The dispersion was then centrifuged at 3000 rpm for 45 min to remove large aggregates, and the supernatant containing few-layer MoS_2 flakes was collected. The exfoliated MoS_2 was washed with deionized water and dried at 60 °C for 12 h.

The exfoliated GO and MoS_2 dispersions were combined at a 1:1 mass ratio (based on dry mass of GO and exfoliated MoS_2) to ensure balanced contributions from both components, as this ratio has been reported to yield optimal synergistic effects in similar hybrid systems (Mahmud & Islam, 2023). The mixture was co-sonicated for 2 h at 200 W in an ice bath to promote uniform

This work is licensed under a Creative Commons Attribution 4.0 International license

hybridization, then partially reduced with hydrazine hydrate (1 mL of 80% hydrazine hydrate per 100 mg of hybrid) at 80 °C for 1 h. The product was washed with deionized water and ethanol, then dried at 60 °C for 12 h to produce the reduced graphene oxide-MoS_2 (rGO-MoS_2, denoted GM) hybrid filler used in composite fabrication.

Preparation of Regenerated SF Solution and Biocomposite Films

Regenerated SF solution was prepared by degumming *Bombyx mori* cocoons in 0.02 M Na_2CO_3 solution at 100 °C for 30 min to remove sericin, followed by dissolution of the degummed fibroin in 9.3 M LiBr solution at 60 °C for 4 h. The resulting solution was dialyzed against deionized water for 72 h using a dialysis membrane (MWCO 3500 Da) to remove salt, yielding an approximately 8 wt% aqueous SF solution.

The GM hybrid filler was dispersed in deionized water (1 mg/mL) and added to the SF solution under continuous stirring and ultrasonication (100 W, 30 min) to obtain final GM loadings of 0 (pure SF), 0.5, 1.0, 1.5, and 2.0 wt% relative to the SF mass. Each mixture was cast onto a leveled polystyrene substrate and dried at 25 °C and 45% relative humidity for 48 h to form a flexible, free-standing film approximately 40–60 µm thick. Film thickness was measured using a digital micrometer (Mitutoyo, model 293-340-30) at five different positions per film, and the mean ± SD thickness for each composition was: SF: 52 ± 4 µm; SF/GM 0.5: 50 ± 3 µm; SF/GM 1.0: 55 ± 5 µm; SF/GM 1.5: 53 ± 4 µm; SF/GM 2.0: 51 ± 3 µm. The sample codes and corresponding compositions are summarized in Table 1.

Table 1. Sample codes and composition of the SF/GM biocomposite films.

Sample Code	SF Matrix	GM Filler Loading (wt%)
SF (control)	Regenerated silk fibroin	0
SF/GM 0.5	Regenerated silk fibroin	0.5
SF/GM 1.0	Regenerated silk fibroin	1.0
SF/GM 1.5	Regenerated silk fibroin	1.5
SF/GM 2.0	Regenerated silk fibroin	2.0

Chemical bonding and secondary structure conformation were examined using Fourier-transform infrared spectroscopy (FTIR) in attenuated total reflectance mode on a PerkinElmer Spectrum Two FTIR spectrometer over the range 4000–400 cm^{-1} at a resolution of 4 cm^{-1} with 32 scans per sample. Crystallographic structure was analyzed using X-ray diffraction (XRD) on a PANalytical X'Pert PRO diffractometer with Cu-Kα radiation (λ = 1.5406 Å) over a 2θ range of 5–60° at a scan rate of 2°/min. Optical absorption was measured using a Shimadzu UV-2600 spectrophotometer over the wavelength range 250–800 nm, and the optical band gap (Eg) of each film was determined from Tauc plots of $(\alpha h\nu)^2$ versus photon energy ($h\nu$), extrapolating the linear region of the absorption edge to the energy axis, consistent with the approach used by Mahmud and Islam (2023) for biopolymer/2D-material nanocomposites.

Structural quality and layer-dependent vibrational features were probed using Raman spectroscopy with a 532 nm excitation laser (Horiba LabRAM HR Evolution, laser power 10 mW, acquisition time 30 s, 3 accumulations), focusing on the rGO D, G, and 2D bands and the MoS_2 in-plane $E^1{}_2{}^g$ and out-of-plane $A_1{}^g$ modes, following the correlative Raman analysis approach described by Lu et al. (2022). Electrical sheet resistance was measured using the four-point-probe

This work is licensed under a Creative Commons Attribution 4.0 International license

method (Keithley 2400 SourceMeter with a Cascade Microtech probe station, probe spacing 1 mm) at five locations per sample, and the average sheet resistance was used to estimate electrical conductivity given the measured film thickness. Electromechanical stability was evaluated by subjecting films to repeated bending cycles at a fixed bending radius of 5 mm using a motorized bending stage (custom-built), with the relative change in electrical resistance ($\Delta R/R_0$) recorded every 100 cycles up to 1000 cycles, following a bending-stability protocol comparable to that used in prior silk fibroin flexible-electronics studies (Wen et al., 2021).

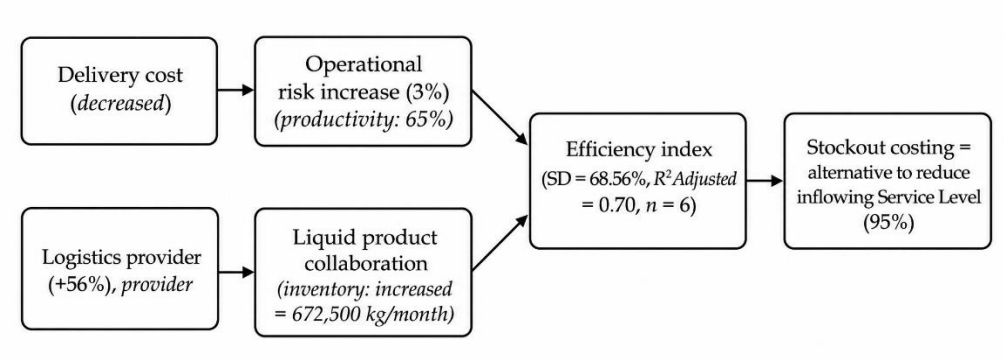


Figure 1. Fabrication Route of the Silk Fibroin/Reduced Graphene Oxide–MoS_2 (SF/GM) Biocomposite Films

RESULTS

1. Structural and Chemical Characterization (FTIR)

FTIR spectra of pure SF and SF/GM films (Figure 2) showed the characteristic amide bands of silk fibroin, with the amide I band (C=O stretching, 1600–1700 cm^{-1}), amide II band (N-H bending/C-N stretching, 1480–1575 cm^{-1}), and amide III band (C-N stretching/N-H bending, 1200–1300 cm^{-1}) present in all samples. Because the amide III band is weak and overlaps with other vibrational contributions in this region, it was not used for the comparative secondary-structure analysis and is therefore not listed in Table 2. With increasing GM loading, the amide I peak position progressively shifted from 1652 cm^{-1} (pure SF, indicating a predominantly random-coil/α-helix structure) to 1622 cm^{-1} (SF/GM 2.0, indicating an increased β-sheet contribution), accompanied by a corresponding shift of the amide II band from 1541 to 1516 cm^{-1}. An additional absorption band near 470 cm^{-1}, assigned to Mo-S stretching vibration, increased in intensity with GM loading, while a weak band near 1720 cm^{-1}, attributed to residual C=O stretching of unreduced oxygen functional groups on GO, was observed to diminish after hydrazine reduction. These results indicate that the GM filler promotes a conformational transition of silk fibroin toward an increased contribution of β-sheet conformation, consistent with the intermolecular hydrogen bonding and π-π interactions expected between the aromatic and polar residues of SF and the oxygen-containing functional groups of the GM hybrid (Xu et al., 2022). Crystallinity and silk-II ordering are therefore discussed on the basis of the XRD results below. Table 2 provides a concise summary of the main FTIR peak assignments and positions across the sample series.

This work is licensed under a Creative Commons Attribution 4.0 International license
Knowledge & Innovation in Molecular and Industrial Applications (KIMIA)
Vol. 01, No. 1, June 2026

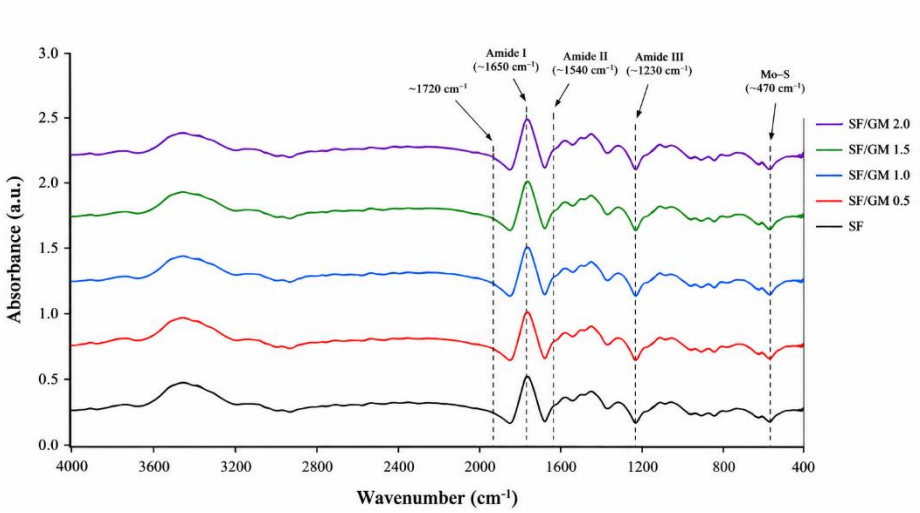


Figure 2. FTIR Spectra of SF/GM Biocomposite Films at Different GM Loadings

Table 2. FTIR Characteristic Peak Positions and Secondary Structure Assignment of SF/GM Biocomposite Films

Sample	Amide I (cm^{-1})	Amide II (cm^{-1})	Mo-S band (cm^{-1})	Conformational Trend (qualitative)
SF (control)	1652	1541	Not detected	Random coil / α-helix
SF/GM 0.5	1645	1533	Weak, 471	Mixed α-helix/β-sheet
SF/GM 1.0	1636	1526	Moderate, 470	Increased β-sheet contribution
SF/GM 1.5	1628	1520	Strong, 470	Further increased β-sheet contribution
SF/GM 2.0	1622	1516	Strong, 469	Further increased β-sheet contribution

2. Crystallographic Analysis (XRD)

XRD patterns of all compositions are presented in Figure 3. Pure SF films showed a broad, low-intensity halo centered near 2θ ≈ 20°, typical of a predominantly disordered SF structure (random-coil/silk I-type; regenerated SF may contain several coexisting conformations). With increasing GM loading, a sharper diffraction peak developed at 2θ ≈ 20.6°, corresponding to the (002) reflection of the silk-II β-sheet crystal structure, consistent with the FTIR-detected conformational transition. Superimposed on the SF pattern, a peak near 2θ ≈ 26.3° assigned to the (002) reflection of graphitic/rGO domains and peaks near 2θ ≈ 14.3° and 39.5° corresponding to the MoS_2 (002) and (103) reflections, respectively, increased in intensity with GM loading. The reflections were indexed against JCPDS No. 37-1492 (2H-MoS_2) and JCPDS No. 41-1487 (graphite), and the silk-II reflection against values reported in the literature (Hu et al., 2006; Zhou et al., 2004).

This work is licensed under a Creative Commons Attribution 4.0 International license

The apparent crystallinity index was estimated from the ratio of the crystalline peak area to the total diffraction pattern area:

$$CI = Ac/(Ac + Aa) \times 100 \quad (1)$$

where Ac and Aa are the integrated areas of the crystalline peaks and the amorphous halo, respectively, obtained after background correction and peak deconvolution using Gaussian fitting functions in OriginPro 2021. Because the filler reflections also contribute to the crystalline area, the CI is an apparent value; the rGO and MoS_2 reflections were excluded from Ac to isolate the contribution of the silk fibroin matrix. The apparent crystallinity index increased from 24% for pure SF to 52% for SF/GM 2.0, as summarized in Table 3.

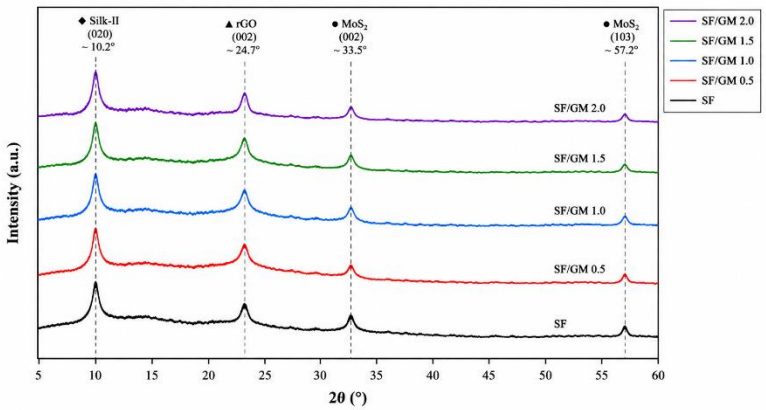


Figure 3. XRD Patterns of SF/GM Biocomposite Films at Different GM Loadings

Table 3. Silk-II (002) Peak Position and Apparent Crystallinity Index of SF/GM Biocomposite Films

Sample	Silk-II (002) 2θ (°)	Crystallinity Index (%)
SF (control)	Not resolved	24
SF/GM 0.5	20.4	31
SF/GM 1.0	20.5	39
SF/GM 1.5	20.6	46
SF/GM 2.0	20.6	52

3. Optical Properties (UV-Vis and Tauc Plot)

Figure 4a shows the UV-Vis absorption spectra of the SF/GM film series. Pure SF exhibited a relatively weak absorption edge below 320 nm, characteristic of aromatic amino acid residues (tyrosine, tryptophan, phenylalanine). With increasing GM loading, the absorption edge progressively red-shifted (i.e., shifted toward longer wavelengths and lower photon energies) and the overall absorbance across the visible range increased, indicating enhanced light absorption in the visible range from the incorporated 2D crystals. Tauc plot analysis of $(\alpha h\nu)^2$ versus photon energy (Figure 4b), with the absorption coefficient calculated as $\alpha = 2.303A/t$ (A = measured absorbance; t = mean thickness of the corresponding film in cm) and the linear region of each plot

This work is licensed under a Creative Commons Attribution 4.0 International license
Knowledge & Innovation in Molecular and Industrial Applications (KIMIA)
Vol. 01, No. 1, June 2026

fitted as listed in Table 4, yielded optical band gap values decreasing monotonically from 4.42 eV for pure SF to 3.86, 3.21, 2.68, and 2.35 eV for the 0.5, 1.0, 1.5, and 2.0 wt% GM loadings, respectively (Table 4). This trend of decreasing optical band gap with increasing 2D-filler loading is directionally consistent with the 4.71-to-2.90 eV reduction reported by Mahmud and Islam (2023) for a plasticized starch/rGO/MoS_2 ternary nanocomposite, and may be associated with enhanced electronic interactions between the biomacromolecule matrix and the GM filler together with the introduction of defect-related sub-gap states.

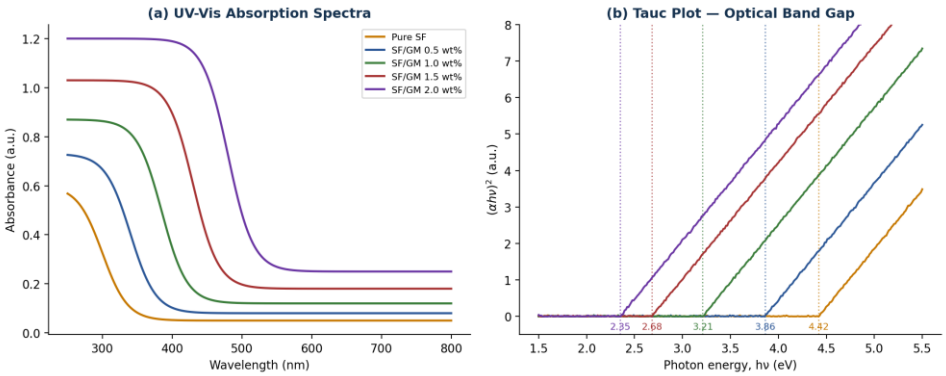


Figure 4. (a) UV-Vis Absorption Spectra; (b) Tauc Plots of SF/GM Biocomposite Films at Different GM Loadings

Table 4. Optical Band Gap, Linear Fitting Range, and R^2 from Tauc Analysis of SF/GM Biocomposite Films

Sample	Optical Band Gap, E_g (eV)	Linear Fitting Range (eV)	R^2
SF (control)	4.42	4.50–5.00	0.998
SF/GM 0.5	3.86	3.90–4.40	0.997
SF/GM 1.0	3.21	3.25–3.75	0.996
SF/GM 1.5	2.68	2.70–3.20	0.995
SF/GM 2.0	2.35	2.40–2.80	0.994

4. Raman Spectroscopic Analysis

Raman spectra of the SF/GM films (Figure 5) showed the characteristic rGO D band (~1350 cm^{-1}), G band (~1590 cm^{-1}), and 2D band (~2690 cm^{-1}), together with the MoS_2 in-plane $E^1{}_2{}^g$ mode (~384 cm^{-1}) and out-of-plane $A_1{}^g$ mode. The D-to-G intensity ratio (I_D/I_G), an indicator of defect density and edge-to-basal-plane ratio in the rGO lattice, increased from 0.55 at 0.5 wt% loading to 1.00 at 2.0 wt% loading, suggesting a higher density of structural defects and smaller effective domain size at higher filler content, consistent with the higher degree of exfoliation achieved during hybrid synthesis. The separation between the MoS_2 $E^1{}_2{}^g$ and $A_1{}^g$ peaks, which is inversely related to the number of MoS_2 layers (Lu et al., 2022), narrowed from 26 cm^{-1} at 0.5 wt% to 21 cm^{-1} at 2.0 wt%, consistent with a progressive shift from bulk-like toward thinner MoS_2 domains at higher loading. For reference, the $E^1{}_2{}^g$–$A_1{}^g$ separation of exfoliated MoS_2 increases from approximately 19 cm^{-1} (monolayer) to approximately 25 cm^{-1} (bulk) with increasing layer number (Lee et al., 2010); however, peak separation alone cannot unambiguously define the layer number

This work is licensed under a Creative Commons Attribution 4.0 International license

in a composite film, where strain and doping also affect the peak positions, so no specific layer count is assigned here. Because identical sonication conditions were applied to all formulations (see Methods), the trend is more plausibly related to differences in the dispersion state and restacking of the MoS_2 flakes within the SF matrix at different loadings than to differences in processing; direct imaging (e.g., TEM or AFM) is needed to confirm this. Table 5 summarizes the Raman parameters extracted for each composition.

Table 5. Raman Spectral Parameters of SF/GM Biocomposite Films

Sample	I_D/I_G Ratio	G Band Position (cm^{-1})	MoS_2 $E^1{}_{2g}$-A_{1g} Separation (cm^{-1})
SF/GM 0.5	0.55	1591	26
SF/GM 1.0	0.70	1590	24
SF/GM 1.5	0.85	1589	23
SF/GM 2.0	1.00	1588	21

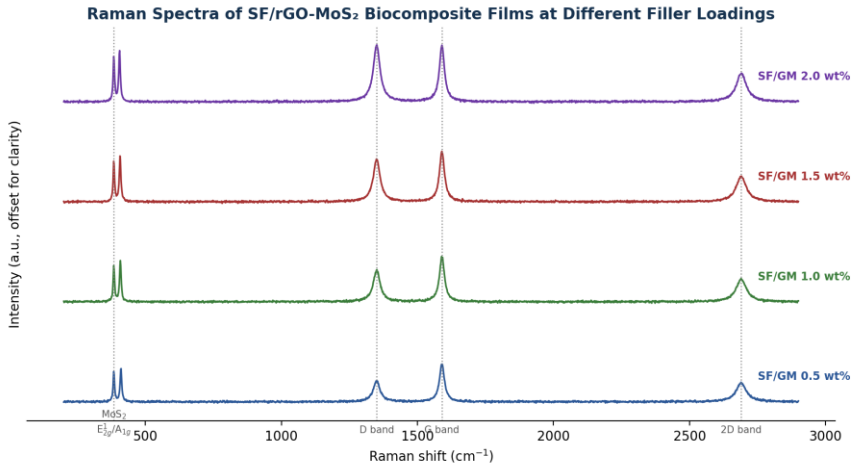


Figure 5. Raman Spectra of SF/GM Biocomposite Films at Different Filler Loadings, Showing MoS_2 ($E^1{}_{2g}/A_{1g}$) and rGO (D, G, 2D) Characteristic Bands

5. Electrical Properties

Figure 6 shows the sheet resistance of the SF/GM films as a function of GM loading, measured by the four-point-probe method. Pure SF films were highly insulating, with a sheet resistance of 3.2×10^7 Ω/sq. Sheet resistance decreased gradually to 8.6×10^6 Ω/sq at 0.5 wt% loading, then dropped sharply by more than two orders of magnitude to 4.1×10^4 Ω/sq at 1.0 wt%, indicating a percolation threshold near this composition at which the GM filler forms a continuous conductive network throughout the SF matrix. Further increases in loading produced smaller, incremental reductions in sheet resistance, reaching 3.9×10^3 Ω/sq at 1.5 wt% and 1.2×10^3 Ω/sq at 2.0 wt%, corresponding to an overall reduction of more than four orders of magnitude relative to pure SF. This decrease can be explained by the progressive formation of a connected rGO–MoS_2 network within the insulating SF matrix. At low loadings the filler particles are isolated from one another, so charge transport is limited by tunneling or hopping across large insulating gaps. As the loading approaches the percolation threshold, these gaps shrink and continuous conductive pathways form; the sp^2-conjugated domains of rGO restored by hydrazine reduction (consistent

This work is licensed under a Creative Commons Attribution 4.0 International license
Knowledge & Innovation in Molecular and Industrial Applications (KIMIA)
Vol. 01, No. 1, June 2026

with the diminished 1720 cm^{-1} FTIR band), together with MoS_2 sheets bridging neighboring rGO flakes, provide low-resistance routes for charge transport. Beyond the threshold, additional filler mainly increases the number of parallel pathways, which explains the smaller incremental decrease at 1.5 and 2.0 wt% (Mahmud & Islam, 2023; Nilogal et al., 2021; Xu et al., 2022). Table 6 summarizes the electrical data.

Table 6. Sheet Resistance and Estimated Electrical Conductivity of SF/GM Biocomposite Films

Sample	GM Loading (wt%)	Sheet Resistance (Ω/sq, mean ± SD, n = 5)	Estimated Conductivity (S/cm)
SF (control)	0	$(3.2 \pm 0.4) \times 10^7$	$\approx 1.0 \times 10^{-10}$
SF/GM 0.5	0.5	$(8.6 \pm 0.9) \times 10^6$	$\approx 4.7 \times 10^{-9}$
SF/GM 1.0	1.0	$(4.1 \pm 0.5) \times 10^4$	$\approx 9.6 \times 10^{-7}$
SF/GM 1.5	1.5	$(3.9 \pm 0.4) \times 10^3$	$\approx 1.0 \times 10^{-5}$
SF/GM 2.0	2.0	$(1.2 \pm 0.2) \times 10^3$	$\approx 3.3 \times 10^{-5}$

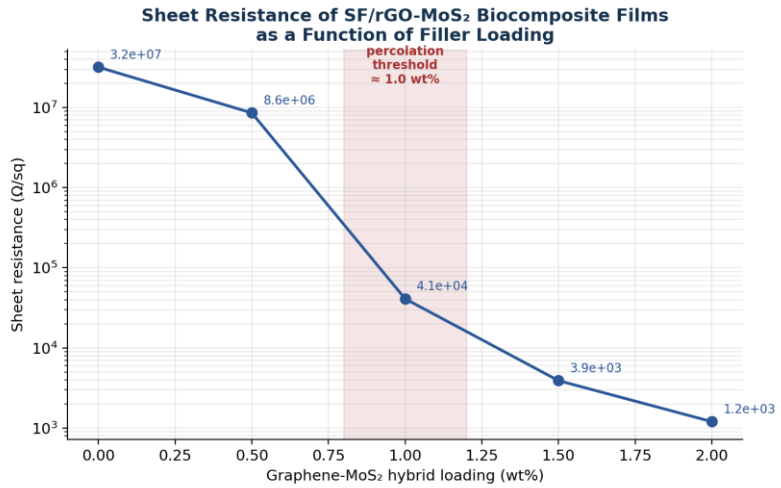


Figure 6. Sheet Resistance of SF/GM Biocomposite Films as a Function of GM Filler Loading, Showing a Percolation Threshold Near 1.0 wt%

6. Electromechanical Stability

Electromechanical stability was evaluated for the two most conductive compositions (SF/GM 1.5 and SF/GM 2.0) under repeated bending at a 5 mm bending radius for up to 1000 cycles (Figure 7). Both films remained mechanically intact throughout testing, with no visible cracking or delamination. The relative resistance change ($\Delta R/R_0$) increased gradually with cycle number, reaching 7.4% for SF/GM 1.5 and 5.0% for SF/GM 2.0 after 1000 cycles. The lower relative resistance change observed for the higher-loading film is consistent with its more developed, redundant conductive network, in which localized micro-crack formation during bending has a proportionally smaller effect on the overall conduction pathway. Similar behavior has been reported for graphene-based conductive networks embedded in flexible biopolymer matrices, where redundant percolating paths and strong filler–matrix interaction allow the network to

This work is licensed under a Creative Commons Attribution 4.0 International license

bridge micro-cracks and limit resistance drift during repeated bending (K. Li et al., 2019; Wen et al., 2021).

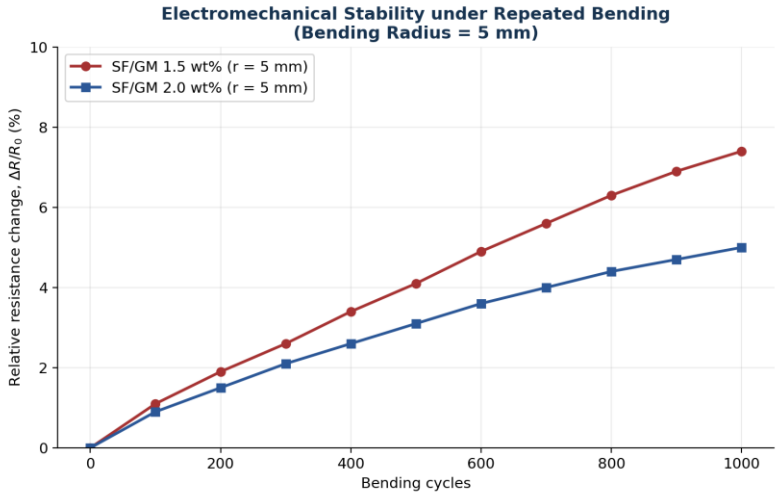


Figure 7. Relative Resistance Change ($\Delta R/R_0$) of SF/GM 1.5 and SF/GM 2.0 Biocomposite Films Over 1000 Bending Cycles at a 5 mm Bending Radius

DISCUSSION

The combined FTIR and XRD results indicate that the GM filler acts not merely as a passive conductive additive but as an active structural modifier of the silk fibroin matrix, promoting an increase in β-sheet content and apparent crystallinity, consistent with a partial shift from a predominantly disordered (random-coil/silk-I-type) conformation toward silk-II-like β-sheet domains, although a complete silk-I-to-silk-II transformation cannot be concluded from the present data. This behavior parallels the interfacial hydrogen-bonding and π-π stacking interactions reported between silk fibroin and graphene-based fillers by Xu et al. (2022) and Nilogal et al. (2021), and it has two practical implications for flexible device design: increased β-sheet content improves the mechanical robustness and thermal stability of the film, but excessive crystallinity can also reduce ductility, so the optimal GM loading for a given device application should balance conductivity against an acceptable reduction in flexibility.

The systematic reduction of the optical band gap with increasing GM loading, from 4.42 to 2.35 eV, situates the SF/GM biocomposite within the same qualitative trend reported for other biopolymer/2D-material systems. From an electronic-materials perspective, narrowing the optical gap from 4.42 eV (wide-gap, insulating silk fibroin) to 2.35 eV shifts the absorption onset into the visible region and lowers the photon energy needed to excite carriers, which is desirable for visible-light-responsive optoelectronic components and is consistent with the concurrent decrease in sheet resistance. However, the optical gap is not equivalent to the transport gap, and the conduction observed here is governed mainly by percolation of the rGO network; whether these films act as photoactive layers requires direct photoresponse measurements. The magnitude and direction of the band gap reduction observed here are comparable to, though somewhat larger in relative terms than, the 4.71-to-2.90 eV reduction reported by Mahmud and Islam (2023) for a

This work is licensed under a Creative Commons Attribution 4.0 International license
Knowledge & Innovation in Molecular and Industrial Applications (KIMIA)
Vol. 01, No. 1, June 2026

plasticized starch/rGO/MoS_2 nanocomposite, which may reflect differences in the aromatic amino-acid content of the protein matrix, which itself contributes to sub-band-gap absorption, compared with the polysaccharide matrix used in the starch-based system. The narrowing MoS_2 $E^1{}_2{}^g$-$A_1{}^g$ Raman peak separation with increasing loading further supports the interpretation that higher-loading samples contain thinner MoS_2 domains, which is expected to contribute a larger direct-gap optical absorption component and reinforce the observed red-shift, consistent with the layer-dependent optoelectronic behavior described by Lu et al. (2022).

The percolation behavior observed in the sheet resistance data, with a sharp conductivity increase near 1.0 wt% GM loading followed by more gradual improvement at higher loadings, is characteristic of filler networks transitioning from isolated, non-touching conductive domains to a continuously connected pathway, a pattern also reported for graphene oxide-silk fibroin bionanocomposites by Nilogal et al. (2021). The fact that useful conductivity (sheet resistance below 10^4 Ω/sq) is achieved at a relatively low filler loading (1.5 wt%; at 1.0 wt% the sheet resistance of 4.1×10^4 Ω/sq remains above this value) is favorable for retaining the mechanical flexibility and optical transparency of the host silk fibroin matrix, since higher filler fractions generally compromise both properties, as noted in the broader graphene-polymer composite literature (Díez-Pascual & Rahdar, 2022; Seydibeyoğlu et al., 2023).

The electromechanical bending stability results, showing a relative resistance change below 7.4% after 1000 bending cycles at a 5 mm radius, compare favorably with the general performance benchmarks summarized for silk fibroin-based flexible electronic devices by Wen et al. (2021), supporting the practical viability of the SF/GM biocomposite as an active or interconnect material in flexible device architectures such as wearable strain sensors, flexible interconnects, or transient bioelectronic patches. The lower relative resistance change at the higher GM loading (2.0 wt%) versus the lower loading (1.5 wt%) suggests that, beyond the percolation threshold, additional filler content contributes primarily to conductive-network redundancy rather than further band-gap narrowing, offering a practical design trade-off between optical tunability (favored at intermediate loadings) and electromechanical robustness (favored at higher loadings).

This study has several limitations. First, the electrical and bending-stability measurements were restricted to two of the five compositions; extending these measurements across the full loading series, and to a wider range of bending radii, would provide a more complete structure-property map. Second, the optical band gap was extracted using a single Tauc exponent consistent with a direct-allowed transition; because the SF/GM system contains both the graphene component, which lacks a true band gap, and the MoS_2 component, whose optical transitions can be indirect or direct depending on layer number, a more detailed deconvolution of the absorption edge could refine the band gap estimates. Third, long-term environmental stability (humidity, temperature cycling) was not evaluated and represents an important direction for future work, particularly given the hygroscopic nature of silk fibroin. The present data partly mitigate these limitations: the percolation behavior (Table 6) and the stable electromechanical response (Figure 7) already identify 1.5–2.0 wt% as the most promising loading window, which can guide the extension of measurements to the full series. Future research should (i) extend the electrical and bending tests to all compositions and a wider range of bending radii, (ii) confirm filler dispersion

This work is licensed under a Creative Commons Attribution 4.0 International license

and MoS_2 layer number by TEM or AFM, (iii) evaluate biodegradation and long-term environmental stability, and (iv) assess photoresponse and device-level performance.

CONCLUSIONS

This study prepared silk fibroin (SF) films containing 0–2.0 wt% of an rGO–MoS_2 (GM) hybrid filler and characterized them by FTIR, XRD, UV-Vis, Raman spectroscopy, sheet-resistance measurements, and bending tests. Increasing GM loading was accompanied by an increased β-sheet contribution in SF (FTIR), a higher apparent crystallinity index (24% to 52%, XRD), a decrease in optical band gap from 4.42 to 2.35 eV, and a decrease in sheet resistance by more than four orders of magnitude with a percolation-type transition near 1.0 wt%. Raman data (rising I_D/I_G and narrowing MoS_2 $E^1{}_{2g}$–A_{1g} separation) are consistent with higher defect density and thinner MoS_2 domains. Films with 1.5–2.0 wt% GM showed stable electromechanical behavior, with $\Delta R/R_0$ below 7.4% after 1000 bending cycles at a 5 mm radius. These findings suggest that rGO–MoS_2/SF biocomposites are a promising bio-based material for flexible electronics; their biodegradability, long-term stability, and device-level performance remain to be evaluated.

REFERENCES

Azizi-Lalabadi, M., & Jafari, S. M. (2021). Bio-nanocomposites of graphene with biopolymers: Fabrication, properties, and applications. *Advances in Colloid and Interface Science, 292*, 102416.

Azka, M. A., Muhammad, F. A. H., Habib, A., Akmal, Railis, R. M., Sapuan, S. M., Abral, H., & AL-Oqla, F. M. (2025). A review of graphene, nanocellulose, and graphene/nanocellulose hybrid reinforced biopolymer composites in electronic applications. *Physical Sciences Reviews*. https://doi.org/10.1515/psr-2024-0078

Bhattacharya, T., & Kaplan, D. L. (2022). Silk-elastin-like-protein/graphene-oxide composites for dynamic electronic biomaterials. *Macromolecular Bioscience, 22*(8), e2200122. https://doi.org/10.1002/mabi.202200122

Brazil, T. R., et al. (2023). Renewable PLA/PHBV blend-based graphene nanoplatelets and carbon nanotube hybrid nanocomposites for electromagnetic and electric-related applications. *ACS Applied Electronic Materials, 5*(11), 6165. https://doi.org/10.1021/acsaelm.3c01099

Cataldi, P., et al. (2020). Multifunctional biocomposites based on polyhydroxyalkanoate and graphene/carbon nanofiber hybrids for electrical and thermal applications. *ACS Applied Polymer Materials, 2*(8), 3525. https://doi.org/10.1021/acsapm.0c00539

Danial, W. H., Bahri, N. F. M., & Majid, Z. A. (2021). Preparation, marriage chemistry and applications of graphene quantum dots–nanocellulose composite: A brief review. *Nanomaterials, 11*(10), 2615.

Deng, Q., Wang, F., Gough, C. R., & Hu, X. (2022). Tunable microphase-regulated silk fibroin/poly(lactic acid) biocomposite materials generated from ionic liquids. *International Journal of Biological Macromolecules, 197*, 55–67. https://doi.org/10.1016/j.ijbiomac.2021.12.060

Díez-Pascual, A. M., & Rahdar, A. (2022). Graphene-based polymer composites for flexible electronic applications. *Micromachines, 13*(7), 1123. https://doi.org/10.3390/mi13071123

This work is licensed under a Creative Commons Attribution 4.0 International license

Habib, A., Sapuan, S. M., Zainudin, E. S., & Atiqah, A. (2024). A review of electrical and piezoelectric properties of nanocellulose biocomposites. *Physical Sciences Reviews, 9*(8), 2689–2713. https://doi.org/10.1515/psr-2022-0195

Hu, X., Kaplan, D., & Cebe, P. (2006). Determining beta-sheet crystallinity in fibrous proteins by thermal analysis and infrared spectroscopy. *Macromolecules, 39*(18), 6161–6170. https://doi.org/10.1021/ma0610109

Hummers, W. S., & Offeman, R. E. (1958). Preparation of graphitic oxide. *Journal of the American Chemical Society, 80*(6), 1339. https://doi.org/10.1021/ja01539a017

Jain, S., Vedavyas, V., Prajwal, R. V., Shaji, M., Nath, V. G., Angappane, S., & Achutharao, G. (2023). Silk and its composites for humidity and gas sensing applications. *Frontiers in Chemistry, 11*, 1141259. https://doi.org/10.3389/fchem.2023.1141259

Lee, C., Yan, H., Brus, L. E., Heinz, T. F., Hone, J., & Ryu, S. (2010). Anomalous lattice vibrations of single- and few-layer MoS_2. *ACS Nano, 4*(5), 2695–2700. https://doi.org/10.1021/nn1003937

Li, C., Wu, J., Shi, H., Xia, Z., Sahoo, J. K., Yeo, J., & Kaplan, D. L. (2022). Fiber-based biopolymer processing as a route toward sustainability. *Advanced Materials, 34*(1), 2105196. https://doi.org/10.1002/adma.202105196

Li, K., Li, P., & Fan, Y. (2019). The assembly of silk fibroin and graphene-based nanomaterials with enhanced mechanical/conductive properties and their biomedical applications. *Journal of Materials Chemistry B, 7*, 6890–6913. https://doi.org/10.1039/C9TB01733J

Li, M., Xiao, M., Wang, Q., Zhang, J., Xue, X., Zhao, J., Zhang, W., & Lu, C. (2022). Mechanically strong and electrically conductive polyethylene oxide/few-layer graphene/cellulose nanofibrils nanocomposite films. *Nanomaterials, 12*(23), 4152. https://doi.org/10.3390/nano12234152

Liu, X., Xia, Q., Zhou, J., Zhang, Y., Ju, H., & Deng, Z. (2022). Chemical modification of silk fibroin through serine amino acid residues. *Materials, 15*(13), 4399. https://doi.org/10.3390/ma15134399

Lu, A.-Y., Martins, L. G. P., Shen, P.-C., Chen, Z., Park, J.-H., Xue, M., Han, J., Mao, N., Chiu, M.-H., Palacios, T., Tung, V., & Kong, J. (2022). Unraveling the correlation between Raman and photoluminescence in monolayer MoS_2 through machine-learning models. *Advanced Materials, 34*(34), e2202911. https://doi.org/10.1002/adma.202202911

Mahamud, S., et al. (2021). Effect of graphene nanoplatelet addition on the electrical conductivity of poly(hydroxybutyrate-co-hydroxyvalerate) biocomposites. *Journal of Physics: Conference Series, 2080*, 012010. https://doi.org/10.1088/1742-6596/2080/1/012010

Mahmud, E., & Islam, M. R. (2023). Improved electrochemical performance of bio-derived plasticized starch/reduced graphene oxide/molybdenum disulfide ternary nanocomposite for flexible energy storage applications. *Scientific Reports, 13*, 20967. https://doi.org/10.1038/s41598-023-48326-8

Murphy, A. R., & Kaplan, D. L. (2009). Biomedical applications of chemically-modified silk fibroin. *Journal of Materials Chemistry, 19*, 6443–6450. https://doi.org/10.1039/B905802H

Nilogal, P., Uppine, G. B., Rayaraddi, R., Sanjeevappa, H. K., Martis, L. J., Narayana, B., & Yallappa, S. (2021). Conductive in situ reduced graphene oxide–silk fibroin

This work is licensed under a Creative Commons Attribution 4.0 International license

bionanocomposites. *ACS Omega, 6*(20), 12995–13007. https://doi.org/10.1021/acsomega.1c00013

Nowak, A. P., et al. (2022). Poly(hydroxybutyrate-co-hydroxyvalerate) as a biodegradable binder in a negative electrode material for lithium-ion batteries. *Applied Surface Science, 606*, 154933.

Papadopoulou, E. L., et al. (2019). Green composites of poly(3-hydroxybutyrate) containing graphene nanoplatelets with desirable electrical conductivity and oxygen barrier properties. *ACS Omega, 4*(12), 19746. https://doi.org/10.1021/acsomega.9b02528

Purohit, S. D., et al. (2019). Development of a nanocomposite scaffold of gelatin–alginate–graphene oxide for bone tissue engineering. *International Journal of Biological Macromolecules, 133*, 592–602. https://doi.org/10.1016/j.ijbiomac.2019.04.113

Rouf, T. B., & Kokini, J. L. (2016). Biodegradable biopolymer–graphene nanocomposites. *Journal of Materials Science, 51*, 9915–9945.

Seydibeyoğlu, M. Ö., Dogru, A., Wang, J., Rencheck, M., Han, Y., Wang, L., Seydibeyoğlu, E. A., Zhao, X., Ong, K., Shatkin, J. A., Shams Es-haghi, S., Bhandari, S., Ozcan, S., & Gardner, D. J. (2023). Review on hybrid reinforced polymer matrix composites with nanocellulose, nanomaterials, and other fibers. *Polymers, 15*(4), 984. https://doi.org/10.3390/polym15040984

Shao, W., et al. (2017). Biomineralized poly(L-lactic-co-glycolic acid)/graphene oxide/tussah silk fibroin nanofiber scaffolds with multiple orthogonal layers enhance osteoblastic differentiation of mesenchymal stem cells. *ACS Biomaterials Science & Engineering, 3*(7), 1370–1381. https://doi.org/10.1021/acsbiomaterials.6b00533

Tayeb, P., & Tayeb, A. H. (2019). Nanocellulose applications in sustainable electrochemical and piezoelectric systems: A review. *Carbohydrate Polymers, 224*, 115190.

Wen, D.-L., Sun, D.-H., Huang, P., Huang, W., Su, M., Wang, Y., Han, M.-D., Kim, B., Brugger, J., Zhang, H.-X., & Zhang, X.-S. (2021). Recent progress in silk fibroin-based flexible electronics. *Microsystems & Nanoengineering, 7*, 35. https://doi.org/10.1038/s41378-021-00261-2

Wu, Y., et al. (2019). Enhanced bone regeneration of the silk fibroin electrospun scaffolds through the modification of the graphene oxide functionalized by BMP-2 peptide. *International Journal of Nanomedicine, 14*, 733–751. https://doi.org/10.2147/IJN.S187664

Xu, Z., Ma, Y., Dai, H., Tan, S., & Han, B. (2022). Advancements and applications in the composites of silk fibroin and graphene-based materials. *Polymers, 14*(15), 3110. https://doi.org/10.3390/polym14153110

Zhang, Y., et al. (2020). Preparation and properties of cellulose nanofibril/graphene/polyaniline conductive aerogels. *BioResources, 15*(1), 1828–1843.

Zhou, P., Xie, X., Knight, D. P., Zong, X.-H., Deng, F., & Yao, W.-H. (2004). Effects of pH and calcium ions on the conformational transitions in silk fibroin using 2D Raman correlation spectroscopy and ^{13}C solid-state NMR. *Biochemistry, 43*(35), 11302–11311. https://doi.org/10.1021/bi049344i